OPTICAL IMAGING POLARIMETRY OF THE LkCa 15 PROTOPLANETARY DISK WITH SPHERE ZIMPOL*

C. Thalmann[1], G. D. Mulders[2], M. Janson[3], J. Olofsson[4,5,6], M. Benisty[7,8], H. Avenhaus[9], S. P. Quanz[1],
H. M. Schmid[1], T. Henning[4], E. Buenzli[4], F. Ménard[10], J. C. Carson[4,11], A. Garufi[1],
S. Messina[12], C. Dominik[13], J. Leisenring[14], G. Chauvin[15], and M. R. Meyer[1]

[1] ETH Zurich, Institute for Astronomy, Wolfgang-Pauli-Strasse 27, 8093 Zurich, Switzerland; thalmann@phys.ethz.ch
[2] Lunar and Planetary Laboratory, The University of Arizona, Tucson, AZ 85721, USA
[3] Department of Astronomy, Stockholm University, SE-106 91, Stockholm, Sweden
[4] Max-Planck-Institut für Astronomie, Königstuhl 17, D-69117 Heidelberg, Germany
[5] Instituto de Física y Astronomía, Facultad de Ciencias, Universidad de Valparaíso, Av.Gran Bretaña 1111, Playa Ancha, Valparaíso, Chile
[6] ICM nucleus on protoplanetary disks, Universidad de Valparaíso, Av. Gran Bretaña 1111, Valparaíso, Chile
[7] Université Grenoble Alpes, IPAG, F-38000 Grenoble, France
[8] CNRS, IPAG, F-38000 Grenoble, France
[9] Departamento de Astronomía, Universidad de Chile, Casilla 36-D, Santiago, Chile
[10] UMI-FCA, CNRS/INSU, France (UMI3386)
[11] Department of Physics & Astronomy, College of Charleston, 66 George Street, Charleston, SC 29424, USA
[12] INAF—Catania Astrophysical Observatory, via S. Sofia 78, I-95123 Catania, Italy
[13] Anton Pannekoek Institute, University of Amsterdam, Science Park 904, 1098 XH Amsterdam, The Netherlands
[14] Steward Observatory, Department of Astronomy, University of Arizona, 933 N. Cherry Avenue, Tucson, AZ 85721, USA
[15] LAOG, 414 Rue de la Piscine, Domaine Universitaire, BP 53, F-38041 Grenoble Cedex 09, France

ABSTRACT

We present the first optical (590–890 nm) imaging polarimetry observations of the pre-transitional protoplanetary disk around the young solar analog LkCa 15, addressing a number of open questions raised by previous studies. We detect the previously unseen far side of the disk gap, confirming the highly off-centered scattered-light gap shape that was postulated from near-infrared imaging, at odds with the symmetric gap inferred from millimeter interferometry. Furthermore, we resolve the inner disk for the first time and trace it out to 30 AU. This new source of scattered light may contribute to the near-infrared interferometric signal attributed to the protoplanet candidate LkCa 15 b, which lies embedded in the outer regions of the inner disk. Finally, we present a new model for the system architecture of LkCa 15 that ties these new findings together. These observations were taken during science verification of SPHERE ZIMPOL and demonstrate this facility's performance for faint guide stars under adverse observing conditions.

Key words: circumstellar matter – planets and satellites: formation – protoplanetary disks – stars: individual (LkCa 15) – stars: pre-main sequence – techniques: high angular resolution

1. INTRODUCTION

Transitional disks are protoplanetary disks with heavily depleted gaps or cavities in their inner regions (e.g., Strom et al. 1989; Calvet et al. 2005). They are thought to represent a transitional state in disk evolution, in which the gas-rich primordial disk gradually disperses due to planet formation or other effects (e.g., Bryden et al. 1999; Owen & Jackson 2012; Alexander et al. 2014).

One transitional disk target that has garnered particular attention in recent years is LkCa 15, a 3–5 Myr old ~1 $M_\odot$ star located approximately 140 pc away (Simon et al. 2000) in the Taurus–Auriga region. A wide gap in the disk extending out to ~50 AU can be inferred from the infrared spectral energy distribution (SED; Espaillat et al. 2007, 2008), but it has also been spatially resolved both in scattered light at near-infrared wavelengths (Thalmann et al. 2010) and in thermal emission at mm/sub-mm wavelengths (Piétu et al. 2007; Andrews et al. 2011; Isella et al. 2014). In near-infrared images, the outer edge of the gap appears off-center from the star, suggesting an eccentric gap (Thalmann et al. 2014), although the mm/sub-mm images are consistent with a circular gap (Andrews et al. 2011; Isella et al. 2014). In addition, Kraus &

Ireland (2012) discovered a protoplanet candidate at ~16–21 AU using Sparse Aperture Masking (SAM). While some follow-up observations only provided upper limits (Isella et al. 2014; Whelan et al. 2015), newest results from Hα differential imaging confirm the accreting protoplanet hypothesis (K. Follette 2015, private communication).

Here we present new scattered-light images of the LkCa 15 disk taken at visible wavelengths using Polarimetric Differential Imaging (PDI). The observations provide better spatial resolution and a more robust determination of the distribution of reflected light from the disk than previous data based on infrared Angular Differential Imaging (ADI), in which forward modeling is necessary to account for self-subtraction effects (Thalmann et al. 2011; Milli et al. 2012; Thalmann et al. 2013).

2. OBSERVATIONS AND DATA REDUCTION

LkCa 15 was observed on two nights during Science Verification Time for the newly commissioned high-contrast imager Spectro-Polarimetric High-contrast Exoplanet REsearch (SPHERE; Beuzit et al. 2008) at the European Southern Observatory's Very Large Telescope facility. Its visible-light instrument, Zurich Imaging POLarimeter (ZIMPOL; Thalmann et al. 2008; Schmid et al. 2012), was used with the extreme adaptive optics system (SAXO; Fusco et al. 2006) to obtain deep imaging polarimetry in the "Very Broad Band" filter

---

spanning the R and I bands (590–890 nm). ZIMPOL offers extreme polarimetric contrast (Schmid et al. 2012) at a pixel scale of 3.6×7.2 mas and a field of view of $3\rlap{.}{''}5 \times 3\rlap{.}{''}5$.

The first observation, on 2015 February 2, comprised seven polarimetric cycles of four half-wave plate positions (Stokes $+Q, -Q, +U, -U$), each exposed for 8×20 s at a time, for a total integration time of 75 minutes. The second observation was executed in the same way on 2015 February 12.

The exposure time had been chosen to saturate the star's point-spread function (PSF) to maximize sensitivity at larger separations. However, the performance of the adaptive optics was poor and highly variable throughout both observations, which rendered the star unsaturated in most frames and yielded a FWHM of ~35 mas ($\approx 2\lambda/D$). This can be ascribed to LkCa 15's apparent magnitude of $R \approx 12$ mag at the faint limit of SAXO's guide star specifications, combined with unfavorable weather conditions and high airmass (~1.5). Furthermore, a "comet-tail" aberration of the PSF core is observed in some frames, likely caused by malfunction of the atmospheric dispersion corrector.

After correcting the raw ZIMPOL data for cosmetics and field distortion, we applied the PDI data reduction method detailed in Avenhaus et al. (2014b). It includes the following steps for reducing instrumental polarization: (1) flux equalization of each simultaneous pair of raw images in order to remove the polarization of the stellar PSF, (2) double-quotient calculation of Stokes Q and U polarized flux images for each polarimetric cycle, (3) empirical correction of polarimetric throughput differences in Stokes Q and U, and (4) empirical correction of angular misalignment of the half-wave plate.

Lastly, we transform the Cartesian coordinate system of the Stokes formalism (Q,U) into a polar coordinate system (Q_ϕ, U_ϕ) in which positive Q_ϕ polarization is defined as azimuthal with respect to the star (Benisty et al. 2015). Under the single-scattering assumption, the scattering polarization should appear in the Q_ϕ image (typically as positive signal), whereas the U_ϕ image should contain no scattered-light signal and can be used to estimate the noise level in the observation (Avenhaus et al. 2014b). While this assumption does not strictly hold for inclined, optically thick disks, as is the case for LkCa 15, the resulting deviations are small and automatically accounted for in the error estimation (Avenhaus et al. 2014a).

Since we find no significant differences between the two epochs, we combine both data sets into one final set of Stokes (I, Q_ϕ, U_ϕ) images, which improves the quality of the results. Since the data are sensitivity-limited, we apply no frame selection. We convolve the polarization images with a circular aperture of 7 pixels (=25 mas) in diameter to reduce shot noise.

3. RESULTS

3.1. Imagery

Our RI-band imaging polarimetry of LkCa 15 is shown in Figure 1. Despite the bad PSF quality, the instantaneous nature of dual-beam polarimetry allowed us to remove the starlight effectively and resolve the LkCa 15 disk at high contrast and unprecedented angular resolution.

The Q_ϕ image reveals a crescent of polarized flux tracing the shape of the near-side edge of the outer disk seen in infrared angular ADI observations (Thalmann et al. 2010, 2014), and a previously unknown bright area of polarized flux surrounding the star at small separations ($\lesssim 0\rlap{.}{''}25$, see panel 1(b)). Both

features appear consistently positive in the Q_ϕ image and are significantly brighter than the residuals in the U_ϕ image at similar radii, which identifies them as scattered light from circumstellar material.

Figure 1(c) provides signal-to-noise ratio (S/N) maps produced by dividing the pixel values of star-centered annuli in the Q_ϕ and U_ϕ images by the standard deviation of the U_ϕ image in the same annuli. Both features achieve S/N values above 5σ over a large number of resolution elements and are therefore detected at high confidence. The inner disk is detected down to a separation of ~1 FWHM (36 mas).

To estimate the dust distribution from the scattered-light intensity, we compensate for the r^{-2} fall-off of the illumination of dust particles with physical distance r from the star. We calculate r for each pixel by deprojecting its apparent distance from the star, assuming its light originates from a plane inclined by $50°$ with its line of nodes at a position angle of $60°$ (cf. Thalmann et al. 2014). Figure 1(d) shows the Q_ϕ and U_ϕ images after multiplying each pixel value with r^2. The disk gap is visible as an abrupt step in brightness at almost all position angles, including the faint far side that had eluded all previous scattered-light observations. The reduced brightness of the disk surface near the minor axis is likely due to the dependence of scattering polarization on the phase angle. However, we note that phase angles should change by at most ~6° along radial paths on the visible disk surface; thus, the location of the gap edge should remain largely unaffected.

The eastern ansa appears brighter than the western one on the 1σ level (evaluated in the r^2-scaled image in 50 pixel diameter apertures).

3.2. Geometric Analysis

ADI observations of circumstellar disks suffer from flux loss and oversubtraction effects (Thalmann et al. 2011, 2013; Milli et al. 2012) and therefore require forward modeling to interpret their results (Thalmann et al. 2014). Imaging polarimetry, on the other hand, yields morphologically sound representations of the disk's appearance in polarized light (e.g., Hashimoto et al. 2011; Garufi et al. 2013; Quanz et al. 2013a, 2013b; Benisty et al. 2015).

We characterize the sharp gap edge in the r^2-scaled Q_ϕ image by fitting it with an ellipse using a modified version of the maximum merit method introduced in Thalmann et al. (2011). We generate a number of ellipses with semimajor and semiminor axes a, b displaced from the star's position by offsets x, y along the two axes, respectively. For a parameter set (a, b, x, y), we consider the two concentric elliptical annuli bounded by the triplet of ellipses $(a - \delta, b - \frac{b}{a}\delta, x, y)$, (a, b, x, y), and $(a + \delta, b + \frac{b}{a}\delta, x, y)$ with an annulus width of $\delta = 10$ pixels (=36 mas = 1 FWHM). The merit function $\eta(a, b, x, y)$ is defined as the mean pixel value in the outer annulus of the r^2-scaled Q_ϕ image minus the mean value of the inner annulus. The best fit is achieved when the merit function is maximized, i.e., where the mean brightness increase from the inner to the outer annulus is greatest. As a measure of uncertainty, we define the "well-fitting" family of ellipses by a threshold of $\eta > \eta_{\max} - \sigma_\eta$, where σ_η is the standard deviation of merits of ellipses in the U_ϕ image.

As demonstrated in Figure 2(a), the best-fit ellipse matches the visual locus of the gap edge convincingly. Its numerical parameters and uncertainties are provided in Table 1.
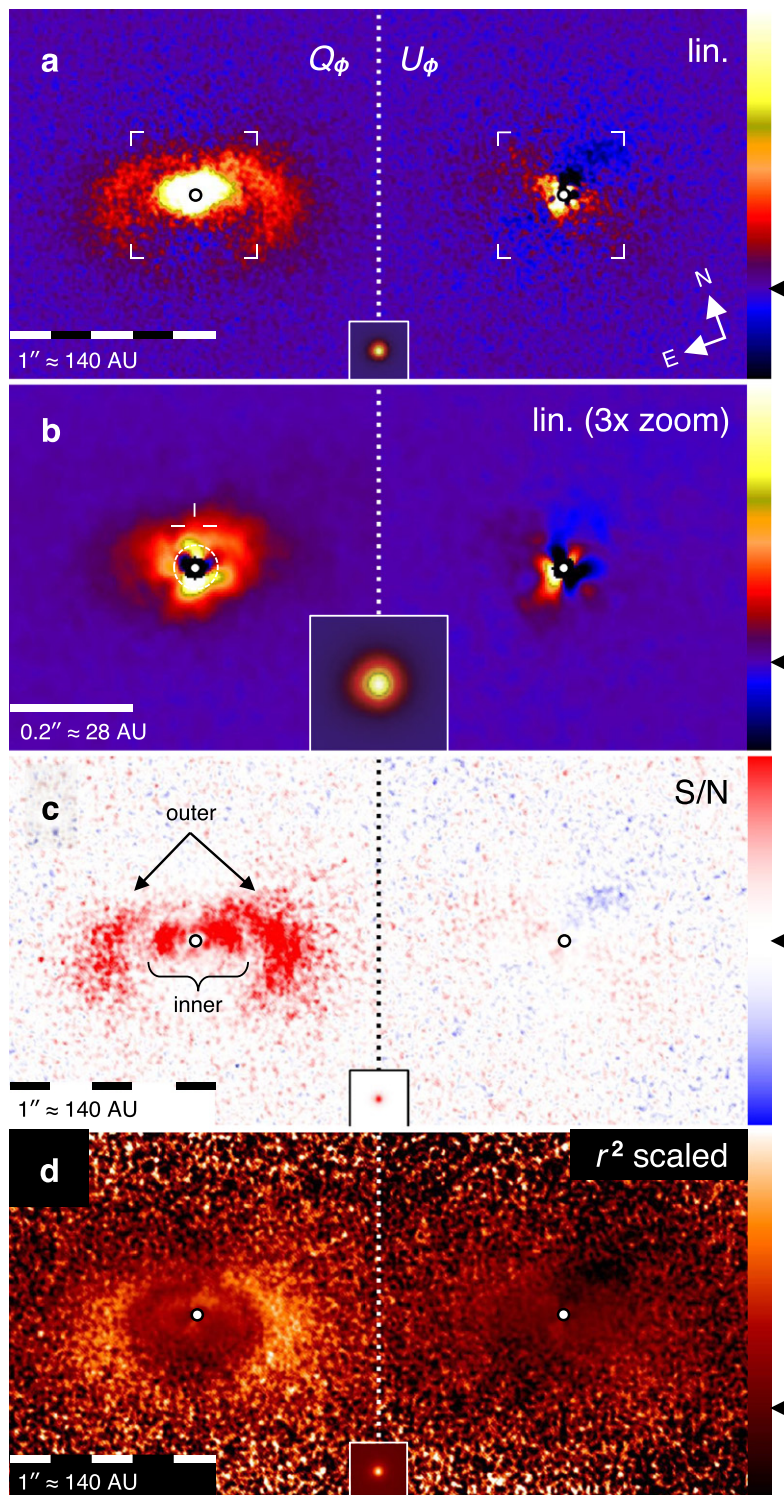
Figure 1. Imaging polarimetry of LkCa 15 based on SPHERE ZIMPOL observations at 590–890 nm. In each panel, the left and right sides show the Q_ϕ and U_ϕ polarized flux images, respectively. Assuming single scattering, the disk appears as positive flux in the Q_ϕ image, while the U_ϕ image provides a noise estimate. All images are convolved with a 7 pixel (=25 mas) diameter circular aperture to reduce shot noise. The small insets show the shape of the PSF core. The location of the star is marked with black-and-white circles. The position angle of the north direction is 30°. The black triangles indicate the zero level in the color scales. (a) Field of view of 1″8 at a linear stretch with a maximum of $\sim 10^{-4}$ times the brightest pixel of the stellar PSF (which is lightly saturated in some of the exposures). The known crescent of scattered light from LkCa 15's outer disk is visible, along with a newly discovered inner disk component close to the star, saturating the color scale. The white corners delimit the area used for (b). (b) The central 0″6 shown at 3x magnification at a linear stretch with a maximum of $\sim 10^{-3}$ times the brightest pixel of the stellar PSF, showing an unsaturated view of the inner disk component. The crosshairs indicate the reported K-band location of LkCa 15 b in Kraus & Ireland (2012). The dashed circle marks the noise-dominated central area. (c) Signal-to-noise ratio (S/N) maps at a stretch of $[-5, 5]\sigma$. The same noise map is used for both the Q_ϕ and U_ϕ images. Both the outer disk and the new inner disk component are detected at high significance. (d) The 1″8 field of view with each pixel multiplied by the square of its de-projected distance from the star, assuming an inclination of 50°.
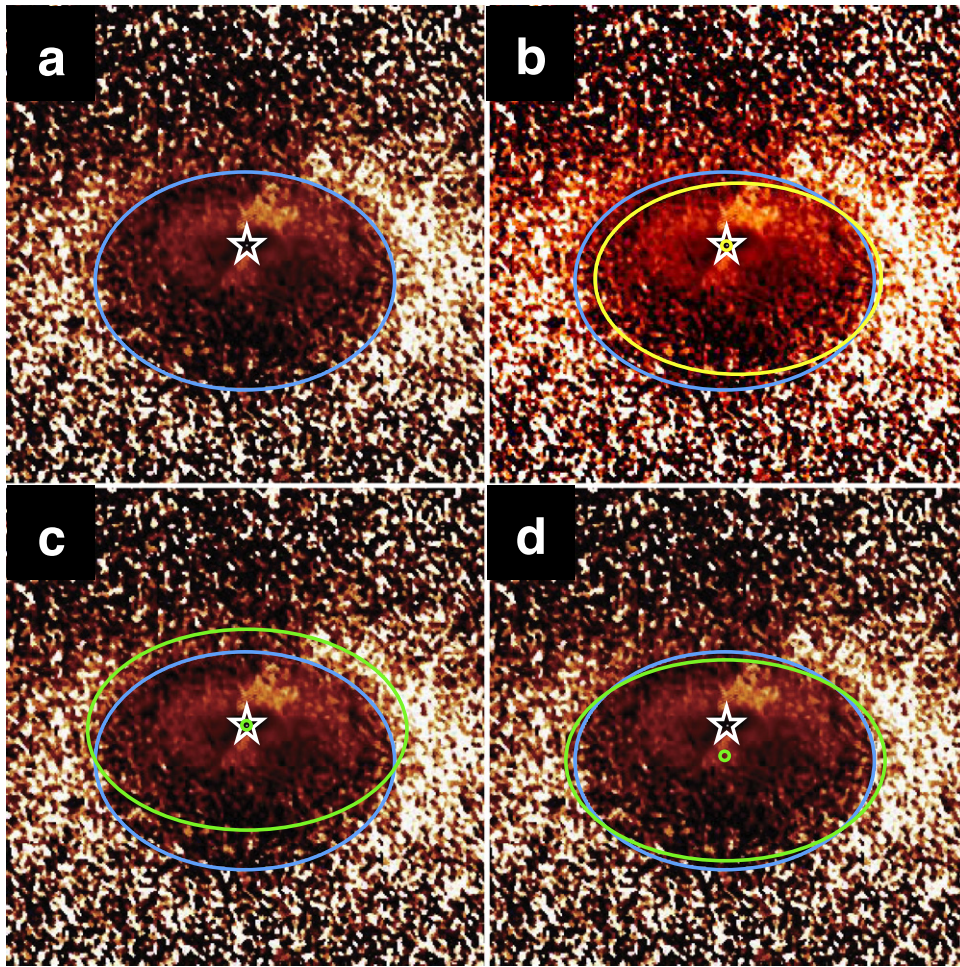
Figure 2. Ellipse fits to the LkCa 15 disk gap edge. The underlying image is the r^2-scaled Q_ϕ image as in Figure 1(d) displayed at a harder stretch, whereas the light blue ellipse represents our fit to its gap (see the text). The location of the star is marked with a star symbol. (a) Visual confirmation of fit for the blue ellipse. (b) Modified maximum merit fit to the best-fit model from the ADI-based forward-modeling analysis in Thalmann et al. (2014) overplotted in yellow. The ellipse is registered against the underlying image by its star position. (c) Fit ellipse (green) to the gap edge in 7 mm emission as reported in Figure 1 of Isella et al. (2014), registered by the assumed star position. (d) The same ellipse as in (c) aligned with our blue fit ellipse, demonstrating that the shapes match well. The small green circle marks the true position of the star relative to the green ellipse.

Table 1
Numerical Results

	In (mas)		In Proj. (AU)	
	Fit Ellipse to the Disk Gap Edge in Q_ϕ			
Semimajor axis a	338	(+11, −18)	47.4	(+1.5, −2.5)
Semiminor axis b	245	(+21, −11)	34.3	(+3.0, −1.5)
Major-axis offset x	−3	(+11, −14)	−0.5	(+1.5, −2.0)
Minor-axis offset y	−79	(+11, −18)	−11.1	(+1.5, −2.5)

|	In (mas)		In Proj. (AU)	
	Characteristic Length Scales of the Inner Scattering Component			
Major axis (east) l_E	69	(+15, −11)	9.7	(+2.1, −1.5)
Major axis (west) l_W	74	(+11, −9)	10.4	(+1.6, −1.2)
Minor axis (north) l_N	51	(+6, −5)	7.2	(+0.9, −0.7)
Minor axis (south) l_S	38	(+10, −6)	5.3	(+1.6, −0.9)

Figure 2(b) compares this fit to a second ellipse obtained by applying the maximum merit method to the best-fit model from our ADI forward-modeling analysis in Thalmann et al. (2014).

The two ellipses share similar sizes, aspect ratios, and significant minor-axis offsets y. However, while we found a marginal major-axis offset x toward the west in Thalmann et al. (2014), our present data are consistent with $x = 0$.

Figure 2(c) shows the ellipse fit to the reconstructed 7 mm emission images reported in Isella et al. (2014) superimposed on our fit. Their ellipse is centered on the star, which results in a significant mismatch with our off-centered ellipse. While the two ellipses can be brought to coincide well with each other by translating one of them by $y \approx 80$ mas (Figure 2(d)), this offset is highly significant compared to the astrometric accuracy of the 7 mm interferometry (10 mas, Isella et al. 2014) and of the ZIMPOL data (<10 mas) and must therefore be physical.

3.3. Surface Brightness Profiles

Figures 3(a) and (b) plot the surface brightness profiles in the Q_ϕ image (without r^2 scaling) along the major and the minor axis, respectively. The plotted values are pixel values as a function of separation averaged over a width of 21 pixels ($=76$ mas) and 81 pixels ($=292$ mas), respectively, and normalized by the brightest pixel value of the star's intensity
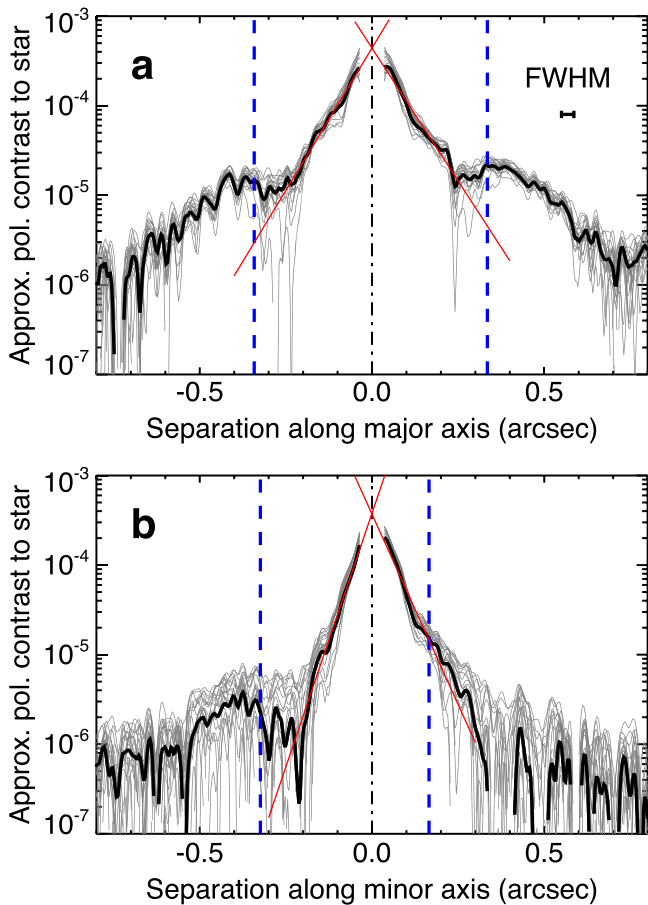
Figure 3. Polarized surface brightness profiles for the LkCa 15 disk. (a) Profile of the Q_ϕ image along the major axis averaged over a width of 21 pixels (=76 mas) centered on the star (thick black curve). The family of thin gray curves are obtained by adding similar profiles taken in the U_ϕ image at various position angles to the black curve, and therefore visualize the noise level in the data. The contrast of a given pixel is calculated by the ratio of its value and the maximum pixel in the stellar full-intensity PSF. The normalization is approximate due to the stellar PSF being saturated in some exposures. The blue dashed lines mark the location of the light blue fit ellipse in Figure 2. The red lines are exponential fits to the inner scattering component. Positive separation values correspond to the western side of the disk. The size of the PSF's FWHM is given for comparison. (b) Profile of the Q_ϕ image along the minor axis averaged over a width of 81 pixels (=292 mas) centered on the star. Positive separation values correspond to the northern side of the disk.

PSF. Since some exposures in the data are saturated, the normalization is only approximate.

The new inner disk component appears as a roughly exponential rise of surface brightness within a radius of ~0″.25. We fit each side of the structure in each of the two profiles as proportional to $\exp(-\theta/l)$, with θ the angular separation from the star and l a characteristic length scale, using least-squares fitting. These fits are listed in Table 1 and illustrated in Figure 3.

To gauge the uncertainty of these results, we extract a number of surface brightness profiles from the noise-like U_ϕ image at various position angles, add each of them to the science profiles from the Q_ϕ image, and recalculate the exponential fits. The standard deviations of these "disturbed" l values are then adopted as the error bars for the table values of l. The disturbed surface brightness profiles are shown in gray in Figure 3.

The polarized intensity is likely underestimated at the innermost separations due to overlapping PSF wings in the Q and U images (Avenhaus et al. 2014a).

4. DISCUSSION

4.1. Inner Disk Component

The newly discovered inner disk component, detected from ~30 AU down to the inner limit of ~7 AU (Figure 3), overlaps with the location of the protoplanet candidate at ~16–21 AU derived from SAM observations (Kraus & Ireland 2012). As with the outer disk, we expect anisotropic scattering to produce a distinct full-intensity forward-scattering maximum on the near side, which coincides with the position angle of the protoplanet candidate. Taken together with the forward-scattering maximum of the outer disk edge (Thalmann et al. 2014), these disk features likely interfere with the reconstruction of SAM data, as in the case of T Cha (Olofsson et al. 2013). However, given the recent Hα detection (K. Follette 2015, private communication), a protoplanet embedded in the inner disk similar to HD100546 b (Quanz et al. 2013a) remains the most plausible interpretation.

The inner disk component also sheds light on the extent of the gap as inferred from previous non-resolved observations. Espaillat et al. (2007) proposed a three-component structure with an outer disk at ~50 AU consistent with the millimeter cavity, an inner disk starting at the dust sublimation radius to explain the near-infrared flux, and an optically thin component out to ~5 AU to explain the prominent silicate emission feature. Our detection of scattered light between 7–30 AU shows illuminated dust is present at these locations above the disk mid plane. An extrapolation of the gap wall temperature ($T \approx 100\,\mathrm{K}/\sqrt{a/a_{\mathrm{wall}}}$) yields a temperature of 150–250 K, consistent with the presence of the 10 and 20 μm silicate emission feature in the SED. We hypothesize that this new scattering structure represents the optically thin part of the inner disk extending out to at least 30 AU. A quick adaptation of the disk model from Mulders et al. (2010) indicates that this can be reconciled with the SED, since the contribution of the optically thin part to the SED is minor. This geometry (narrow gap, depleted inner disk, millimeter cavity) qualitatively matches the imprint of a single planet on a disk (e.g., Jang-Condell & Turner 2012; Zhu et al. 2012).

4.2. Off-centered Gap

Our *RI*-band polarimetry confirms the prediction from *K*-band ADI forward-modeling (Thalmann et al. 2014) that the outer boundary of the gap in the LkCa 15 disk appears off-centered in reflected light, with a highly significant offset of $y \approx 80$ mas (a third of the gap's projected radius) between the star and the gap's apparent center. While disk gaps are known to vary in size as a function of observed wavelength in systems with planet-induced dust filtering (de Juan Ovelar et al. 2013), a lateral displacement of the gap is more difficult to justify and has not been predicted by numerical simulations.

The outer disk's vertical structure cannot account for this displacement since the gap wall profile is tapered ("round") rather than vertical (Thalmann et al. 2014). This is qualitatively confirmed by the wide, homogeneous distribution of scattered light in Figure 1(d).

Another explanation is provided by shadowing. Espaillat et al. (2007) originally proposed an inner disk coplanar with
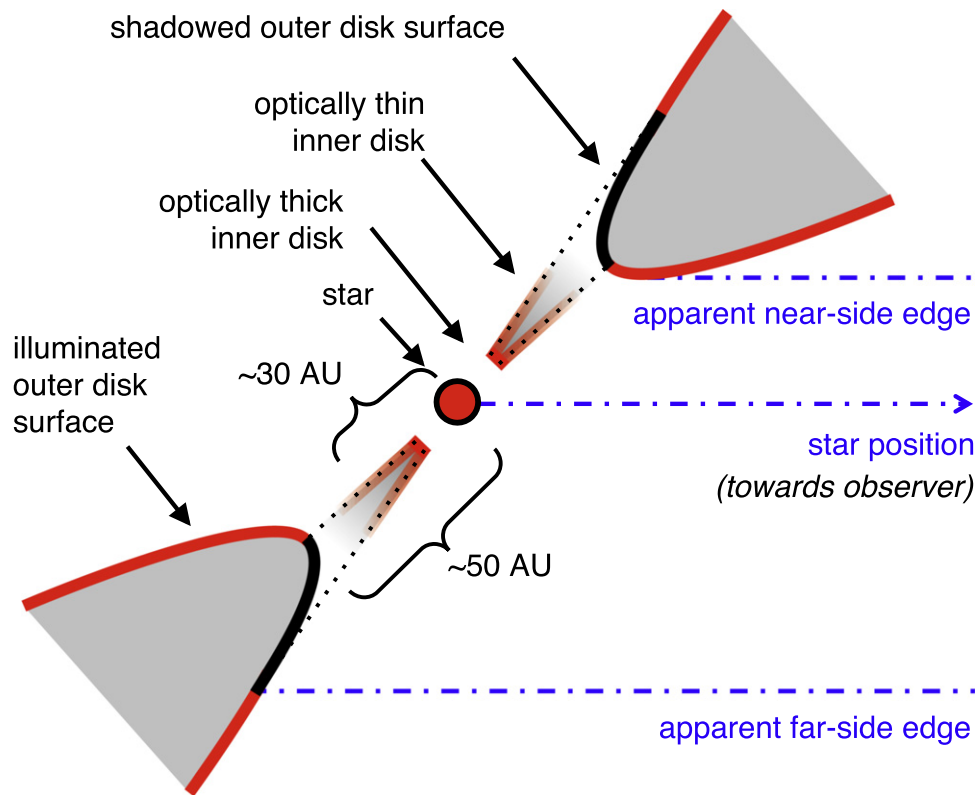
Figure 4. Schematic of the proposed architecture of the LkCa 15 disk (not to scale). Red lining marks the disk surfaces illuminated by the star. Dotted black lines trace the edges of the shadow cast by the inner disk.

the outer disk, casting a shadow onto the outer disk's inner wall Mulders et al. (2010). Our forward modeling in Thalmann et al. (2014) achieved significantly better fits with an unshadowed gap wall, which led us to speculate that the inner disk—and its shadow—were tilted out of the outer disk's plane. On the other hand, this arrangement should result in dark lanes cutting across the outer disk where the shadow plane intersects it, as seen in HD 142527 (Marino et al. 2015). No such lanes are apparent in the LkCa 15 imagery.

This conundrum can be resolved if the inner disk has a slightly higher inclination than the outer disk (Figure 4). The near-side disk rim as observed from Earth would then be fully exposed to stellar irradiation, whereas the far-side disk surface would be obscured at the rim and only become visible further out where the disk surface flares out of the shadow. This would create an off-centered apparent gap in reflected light even with a symmetric physical disk gap. For the disk architecture in Thalmann et al. (2014), the requisite differential tilt would be of order 1°, which could be induced by a planet on a tilted orbit (cf. Mouillet et al. 1997; Augereau et al. 2001; Lagrange et al. 2012).

A similar effect could be caused by a shadowing structure vertically extending from an otherwise coplanar inner disk (Espaillat et al. 2011), though this would imply dramatic variability on the timescale from days to years. While we cannot exclude this possibility, we find no significant variability in our observations (Thalmann et al. 2014; this work).

We thank A. Isella and the anonymous referee for helpful correspondence. This work has been carried out within the frame of the National Centre for Competence in Research

REFERENCES

Alexander, R., Pascucci, I., Andrews, S., Armitage, P., & Cieza, L. 2014, Protostars and Planets VI (Tucson, AZ: Univ. Arizona Press)
Andrews, S. M., Rosenfeld, K. A., Wilner, D. J., & Bremer, M. 2011, ApJL, 742, L5
Augereau, J. C., Nelson, R. P., Lagrange, A. M., Papaloizou, J. C. B., & Mouillet, D. 2001, A&A, 370, 447
Avenhaus, H., Quanz, S. P., Meyer, M. R., et al. 2014a, ApJ, 790, 56
Avenhaus, H., Quanz, S. P., Schmid, H. M., et al. 2014b, ApJ, 781, 87
Benisty, M., Juhasz, A., Boccaletti, A., et al. 2015, arXiv:1505.05325
Beuzit, J.-L., Feldt, M., Dohlen, K., et al. 2008, Proc. SPIE, 7014, 701418
Bryden, G., Chen, X., Lin, D. N. C., Nelson, R. P., & Papaloizou, J. C. B. 1999, ApJ, 514, 344
Calvet, N., D'Alessio, P., Watson, D. M., et al. 2005, ApJL, 630, L185
de Juan Ovelar, M., Min, M., Dominik, C., et al. 2013, A&A, 560, A111
Espaillat, C., Calvet, N., D'Alessio, P., et al. 2007, ApJL, 670, L135
Espaillat, C., Calvet, N., Luhman, K. L., Muzerolle, J., & D'Alessio, P. 2008, ApJL, 682, L125
Espaillat, C., Furlan, E., D'Alessio, P., et al. 2011, ApJ, 728, 49
Fusco, T., Rousset, G., Sauvage, J.-F., et al. 2006, OExpr, 14, 7515
Garufi, A., Quanz, S. P., Avenhaus, H., et al. 2013, A&A, 560, A105
Hashimoto, J., Tamura, M., Muto, T., et al. 2011, ApJL, 729, L17
Isella, A., Chandler, C. J., Carpenter, J. M., Pérez, L. M., & Ricci, L. 2014, ApJ, 788, 129
Jang-Condell, H., & Turner, N. J. 2012, ApJ, 749, 153
Kraus, A. L., & Ireland, M. J. 2012, ApJ, 745, 5
Lagrange, A.-M., Boccaletti, A., Milli, J., et al. 2012, A&A, 542, A40
Marino, S., Perez, S., & Casassus, S. 2015, ApJL, 798, L44
Milli, J., Mouillet, D., Lagrange, A.-M., et al. 2012, A&A, 545, A111

Mouillet, D., Larwood, J. D., Papaloizou, J. C. B., & Lagrange, A. M. 1997, MNRAS, 292, 896

Mulders, G. D., Dominik, C., & Min, M. 2010, A&A, 512, A11

Olofsson, J., Benisty, M., le Bouquin, J.-B., et al. 2013, A&A, 552, A4

Owen, J. E., & Jackson, A. P. 2012, MNRAS, 425, 2931

Piétu, V., Dutrey, A., & Guilloteau, S. 2007, A&A, 467, 163

Quanz, S. P., Amara, A., Meyer, M. R., et al. 2013a, ApJL, 766, L1

Quanz, S. P., Avenhaus, H., Buenzli, E., et al. 2013b, ApJL, 766, L2

Schmid, H.-M., Downing, M., Roelfsema, R., et al. 2012, Proc. SPIE, 8446, 84468Y

Simon, M., Dutrey, A., & Guilloteau, S. 2000, ApJ, 545, 1034

Strom, K. M., Strom, S. E., Edwards, S., Cabrit, S., & Skrutskie, M. F. 1989, AJ, 97, 1451

Thalmann, C., Grady, C. A., Goto, M., et al. 2010, ApJL, 718, L87

Thalmann, C., Janson, M., Buenzli, E., et al. 2011, ApJL, 743, L6

Thalmann, C., Janson, M., Buenzli, E., et al. 2013, ApJL, 763, L29

Thalmann, C., Mulders, G. D., Hodapp, K., et al. 2014, A&A, 566, A51

Thalmann, C., Schmid, H. M., Boccaletti, A., et al. 2008, Proc. SPIE, 7014, 70143F

Whelan, E. T., Huelamo, N., Alcala, J. M., et al. 2015, arXiv:1504.04824

Zhu, Z., Nelson, R. P., Dong, R., Espaillat, C., & Hartmann, L. 2012, ApJ, 755, 6